Supplement of Atmos. Chem. Phys., 26, 6471–6487, 2026
https://doi.org/10.5194/acp-26-6471-2026-supplement

Atmospheric Chemistry and Physics
Open Access
EGU

Supplement of

Interpretable machine learning quantifies composition and size influences on aerosol spectral absorption

Wenfang Wang et al.

Correspondence to: Pengfei Tian (tianpf@lzu.edu.cn) and Min Chen (chenmin@lzu.edu.cn)

S1. Stokes Diameter Conversion Aerodynamic Diameter.

SMPS used 8.82-310.6 nm data and APS used 0.523-19.81 μm data. For particle density of 1.7 g·cm^{-3} the particle diameter 310.6 nm corresponds to the aerodynamic diameter $D_a = \sqrt{\rho_p/\rho_0}\, D_p \cong 405\, nm$, where ρ_0 = 1 g·cm^{-3}, and ρ =1.7 g·cm^{-3} is constant over the whole size range (Shang et al., 2018).

S2. Offline chemical analysis of filter samples.

For WSII, one quarter of each filter was cut into small pieces and extracted with 10 mL ultrapure water (>18 MΩ·cm) by ultrasonication for 30 min; the extraction was repeated once, and the combined extracts were brought to 25 mL with ultrapure water. The extract was filtered through a 0.45 μm membrane (GHP, model 4563, Pall Inc., USA) and stored at 4 °C prior to ion chromatography (881 Compact IC Pro, Metrohm, Switzerland; and ICS-1500, Dionex Inc., USA). Cations (Na^+, K^+, NH_4^+, Ca^{2+}, Mg^{2+}) were measured with ion chromatograph (881 Compact IC Pro, Metrohm, Switzerland) equipped with a Metrosep C4 column. The eluent was 1.75 mM HNO_3 + 0.75 mM dipicolinic acid. Anions (Cl^-, NO_3^-, SO_4^{2-}) were measured with an ion chromatograph (ICS-1500, Dionex Inc., USA) equipped with an IonPac AS22 column. The eluent was 4.5 mM Na_2CO_3 + 1.4 mM $NaHCO_3$. The method detection limits (MDLs) were 0.05, 0.10, 0.19, 0.04, 0.01, 0.02, and 0.02mg·L^{-1} for K^+, NH_4^+, Ca^{2+}, Mg^{2+}, Cl^-, NO_3^-, and SO_4^{2-}, respectively. Due to generally elevated Na^+ blanks associated with quartz-fiber filters and glassware, Na^+ was excluded here.

One quarter of each quartz-fiber filter was used for elemental analysis. The filter portion was cut into small pieces and transferred to a digestion bottle. Concentrated nitric acid (HNO_3, 68%, 10 mL) was added, and the mixture was heated until digestion was complete. After cooling, the digest was diluted to 20 mL with ultrapure water. The resulting solutions were analyzed for Al, Ca, Mg, Fe, and Ti using inductively coupled plasma–atomic emission spectrometry (ICP-AES; iCAP 7400, Thermo, USA). The MDLs were 0.02, 0.19, 0.02, 0.07, and 0.00 $mg \cdot L^{-1}$ for Al, Ca, Mg, Fe, and Ti, respectively.

A circular area of each filter sample using a 0.504 cm^2 punch was cut for the analysis of OC and EC by thermal/optical carbon analyzer (DRI Model 2015, USA) following the thermal/optical reflectance (TOR) method (Chow et al., 2007). Briefly, a filter punch was progressively heated to evolve carbon fractions under stepwise temperature programs. OC fractions were evolved in a pure He atmosphere at 120 °C (OC1), 250 °C (OC2), 450 °C (OC3), and 550 °C (OC4). Subsequently, EC fractions were evolved in an oxidizing atmosphere of 2% O_2 and 98% He at 550 °C (EC1), 700 °C (EC2), and 800 °C (EC3). Evolved carbon was oxidized to CO_2 and then reduced to CH_4 for detection using a flame ionization detector. Pyrolyzed organic carbon (OPC) was monitored using the laser reflectance signal and was defined when the reflected laser signal returned to its initial value after the introduction of O_2 into the analysis atmosphere. OC was calculated as OC1 + OC2 + OC3 + OC4 + OPC, whereas EC was calculated as EC1 + EC2 + EC3 − OPC. The MDLs were 0.18 and 0.04 $\mu g \cdot m^{-2}$

for OC and EC, respectively.

S3. Mie theory sensitivity experiments.

To provide a physical consistency check for the SHAP-based attribution, we conducted a set of Mie-theory sensitivity experiments to isolate how (i) short-wavelength absorptivity and (ii) particle-size structure can influence the absorption Ångström exponent between 440 and 870 nm. The experiments use the AERONET-retrieved column volume size distribution (VSD), expressed as $\frac{dV}{dlnr}$ on a discrete radius grid r spanning approximately 0.05–15μm. For each radius bin, the number size distribution is obtained by

$$\frac{\mathrm{dN}}{dlnr} = \frac{1}{\frac{4}{3}\pi r^3} \times \frac{dV}{dlnr} \tag{S1}$$

Given the complex refractive index $m = n - ik$, where n is the real part and k is the imaginary part, we compute the absorption efficiency $Q_{abs}(r, \lambda)$ using Mie theory (Bohren and Huffman, 1983). The AAOD at wavelength λ is then evaluated by integrating absorption cross section (up to a proportionality constant) weighted by the number distribution,

$$AAOD_\lambda \propto \int Q_{abs}(r,\lambda)\, \pi r^2 \frac{\mathrm{dN}}{dlnr} dlnr \tag{S2}$$

Because our goal is sensitivity and mechanistic consistency rather than an exact retrieval of absolute AAOD, the proportionality constant is not required; all comparisons are made within the same computational framework. The AAE between 440 and 870 nm is computed as

$$AAE = -\frac{ln(\frac{AAOD_{440}}{AAOD_{870}})}{ln(\frac{440}{870})} \quad \text{(S3)}$$

To isolate the influence of composition-related changes, we varied only the imaginary refractive index at 440 nm (k_{440}) while holding the size distribution fixed. Specifically, k_{440} was scaled by multiplicative factors of 0.6, 0.8, 1.0, 1.2, and 1.5, while k_{870} was kept unchanged. The real part n was held constant in these tests (1.5, the mean AERONET-retrieved value). This design emphasizes changes in absorption that preferentially affect shorter wavelengths, consistent with increased contributions from aerosol components that absorb more strongly in the near-UV (e.g., absorbing mineral dust and brown carbon), and avoids conflating this effect with broadband absorbers whose spectral dependence is weak.

To isolate the role of particle-size structure, we held the refractive index fixed and perturbed the size distribution by shifting the characteristic radii of the fine and coarse modes. We separated the VSD into a fine subset and a coarse subset using a radius threshold of r = 0.6 μm. For each subset, we performed a log-radius shift,

$$\left(\frac{dV}{dlnr}\right)_{new}(\mathrm{r}) = \left(\frac{dV}{dlnr}\right)_{old}(\frac{\mathrm{r}}{s}) \quad \text{(S4)}$$

where s is the shift factor. We used s = 0.8,0.9,1.0,1.1, and 1.2, corresponding to moving the characteristic radius to 80%, 90%, 100%, 110%, and 120% of the baseline value. The shift is implemented by linear interpolation in lnr, with values outside the original subset radius range set to zero. To ensure that this perturbation represents a change in size location rather than loading, we renormalize the shifted subset so that its

mode-integrated volume is conserved,

$$\int \left(\frac{dV}{dlnr}\right)_{new} dlnr = \int \left(\frac{dV}{dlnr}\right)_{old} dlnr \quad \text{(S5)}$$

The unperturbed subset is kept unchanged, so that "fine-mode shift" modifies only the fine subset while the coarse subset remains fixed, and vice versa for "coarse-mode shift". The resulting sensitivity curves are summarized in Fig. S11.

Table S1. Correlation Matrix of Aerosol Chemical Species

	NH_4^+	K^+	Mg^{2+}	Ca^{2+}	Cl^-	SO_4^2	NO_3^-	OC	EC	Al	Ca	Fe	Mg	Ti
NH_4^+	1.00	0.90	0.25	-0.07	0.50	0.95	0.99	0.83	0.78	0.08	0.07	0.34	0.23	0.20
K^+		1.00	0.36	-0.07	0.52	0.85	0.89	0.84	0.82	0.03	-0.03	0.24	0.20	0.09
Mg^{2+}			1.00	0.76	0.74	0.24	0.23	0.35	0.33	0.30	0.31	0.03	0.34	0.08
Ca^{2+}				1.00	0.33	-0.05	-0.07	-0.06	-0.05	0.11	0.11	-0.15	0.11	-0.09
Cl^-					1.00	0.45	0.48	0.57	0.54	0.35	0.39	0.13	0.40	0.18
SO_4^{2-}						1.00	0.95	0.76	0.72	0.09	0.08	0.27	0.19	0.21
NO_3^-							1.00	0.82	0.77	0.07	0.06	0.34	0.23	0.19
OC								1.00	0.82	0.10	0.10	0.35	0.22	0.08
EC									1.00	0.00	-0.02	0.14	0.12	0.00
Al										1.00	0.88	0.07	0.91	0.11
Ca											1.00	0.15	0.86	0.20
Fe												1.00	0.11	0.60
Mg													1.00	0.07
Ti														1.00

Table S2. Summary statistics of standardized MLR coefficients and model performance from 1000 bootstrap resamples for the extended model specifications.

coef	mean	std	p2.5	p97.5
a	0.006633	0.069351	-0.12142	0.148516
EC	-7.5E+11	9.37E+11	-2.7E+12	9.93E+11
OM	-2.1E+12	2.57E+12	-7.3E+12	2.73E+12
FMD	-7.3E+12	9.12E+12	-2.6E+13	9.67E+12
nd-WSII	-7.1E+12	8.9E+12	-2.5E+13	9.43E+12
D_{SMPS}	0.032792	0.125148	-0.18773	0.299769
D_{APS}	0.446719	0.086028	0.300897	0.630525
R^2	0.74	0.03	0.67	0.77
RMSE	0.13	0.01	0.13	0.15
MAE	0.10	0.01	0.09	0.16

The extended model refers to the standardized MLR specification including EC and OM fractions. coef denotes the regression coefficient (including the intercept term, “a”). mean and std are the bootstrap mean and standard deviation of each coefficient across 1000 resamples. p2.5 and p97.5 are the 2.5th and 97.5th percentiles of the bootstrap distribution, respectively, forming the percentile-based 95% bootstrap confidence interval.

Table S3. Summary statistics of standardized MLR coefficients and model performance from 1000 bootstrap resamples for the reduced model specifications.

coef	mean	std	p2.5	p97.5
a	0.00	0.07	-0.13	0.14
FMD	0.35	0.17	0.04	0.71
nd-WSII	-0.16	0.17	-0.50	0.17
D_{SMPS}	-0.02	0.12	-0.24	0.26
D_{APS}	0.44	0.09	0.30	0.64
R^2	0.74	0.02	0.68	0.76
RMSE	0.13	0.01	0.13	0.15
MAE	0.10	0.01	0.09	0.11

The reduced model refers to the standardized MLR specification excluding EC and OM fractions.

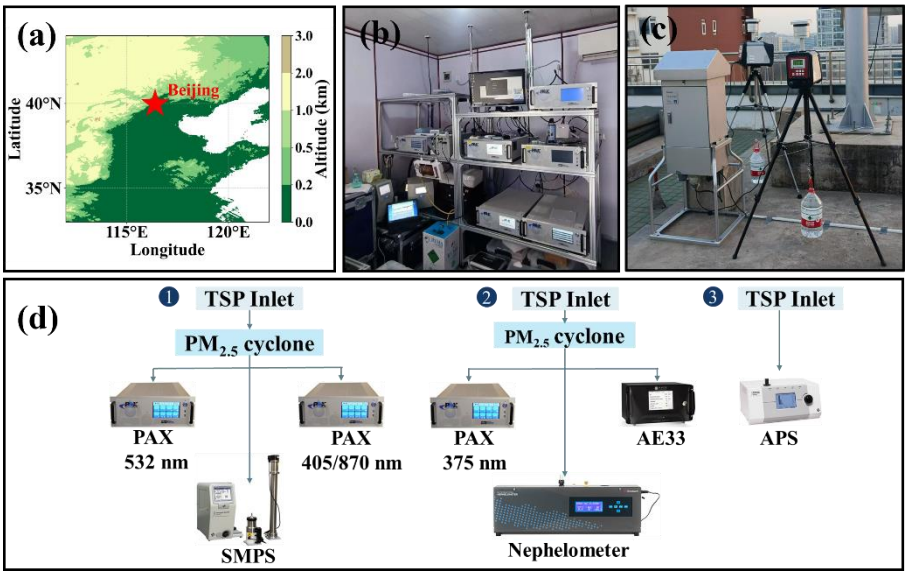

Figure S1. Geographic location of observation site and observation instruments. (a) Geographical map, location of the field campaign. (b, c) Photographs during the field campaign. (d) Airflow settings of the online instruments.

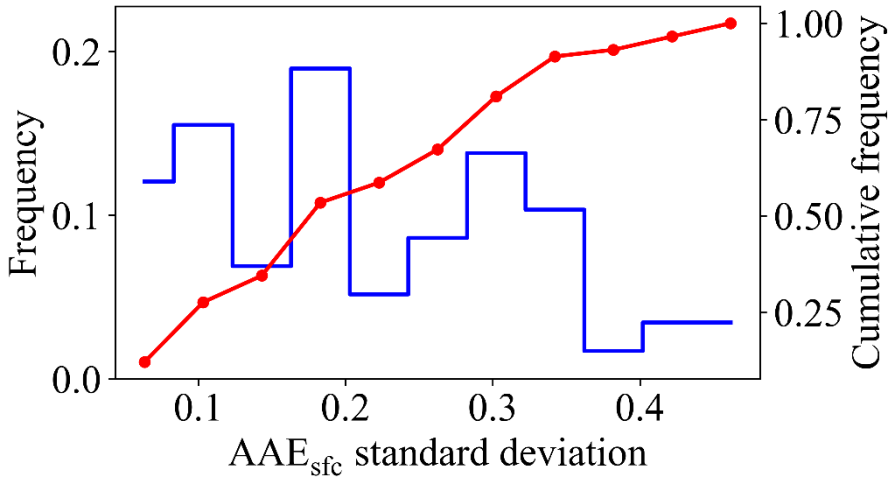

109

110 **Figure S2**. Frequency (blue) and cumulative frequency (red) distributions of within-
111 window AAE_{sfc} standard deviation (11.5 h).

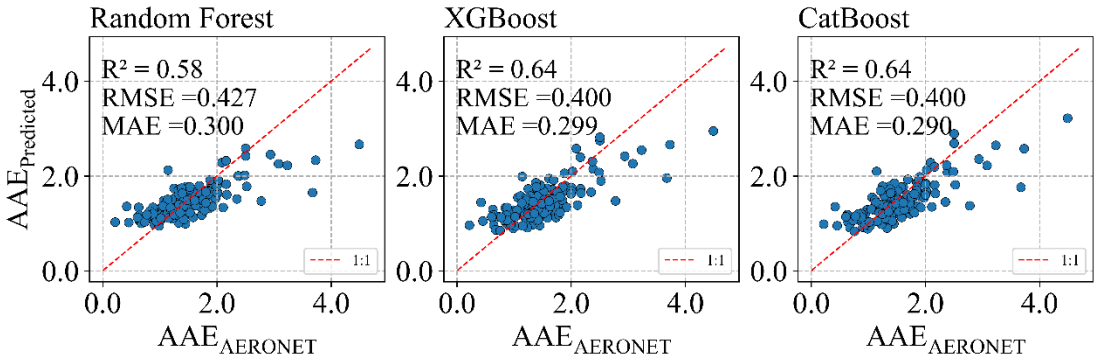

112

113 **Figure S3.** Comparison of aerosol absorption Ångström exponent (AAE) predictions
114 and AERONET observations by different models.

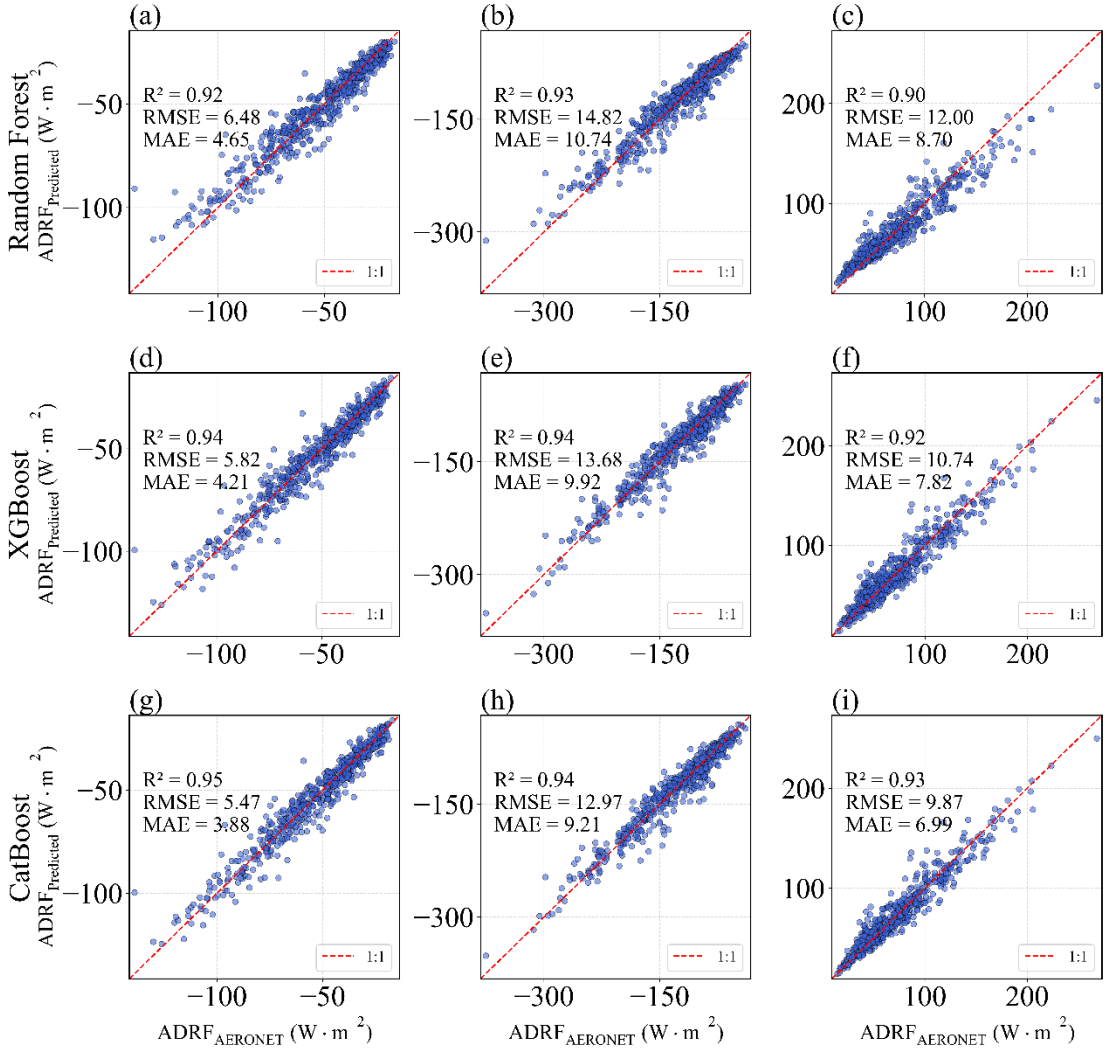

Figure S4. Comparison of aerosol direct radiative forcing (ADRF) predictions and AERONET observations by different models.

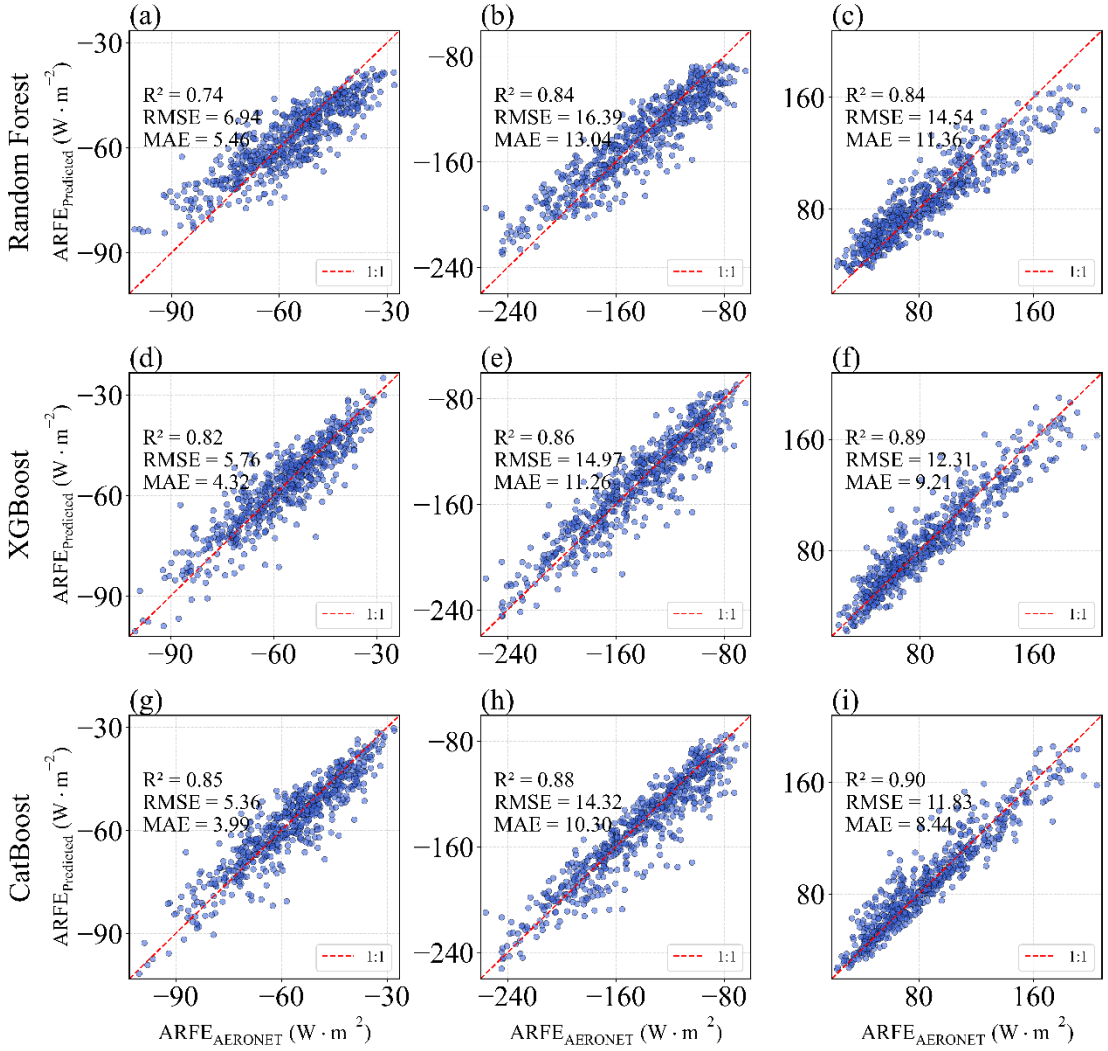

118

119 **Figure S5.** Comparison of aerosol radiative forcing efficiency (ARFE) predictions and

120 AERONET observations by different models.

121

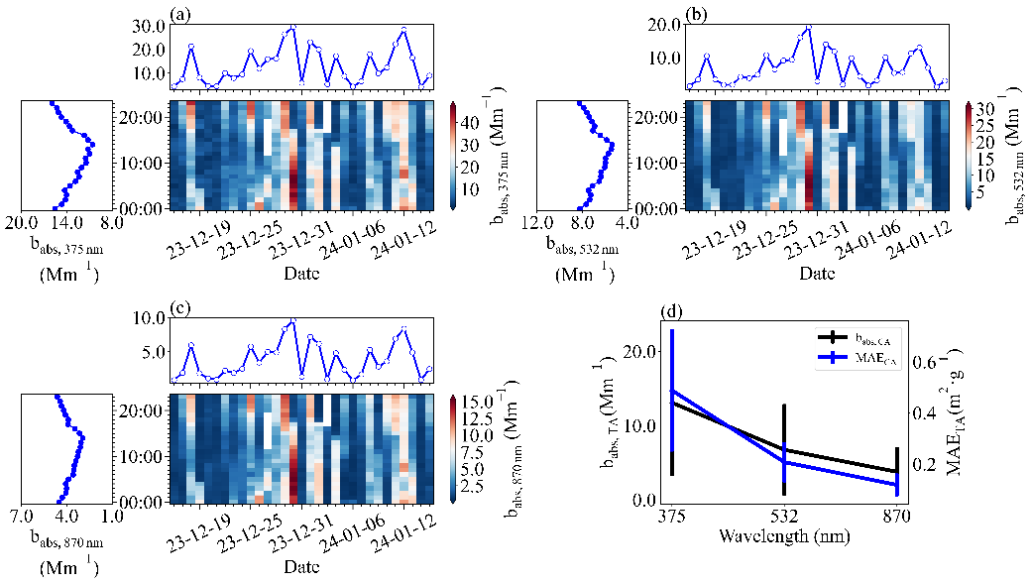

122

123 **Figure S6.** (a, b, c) The time series of mass concentrations of absorption coefficients at
124 375, 405, 870 nm, mass absorption efficiency at 375, 405, 870 nm. (d). Wavelength
125 dependence of absorption coefficients and mass absorption efficiency.

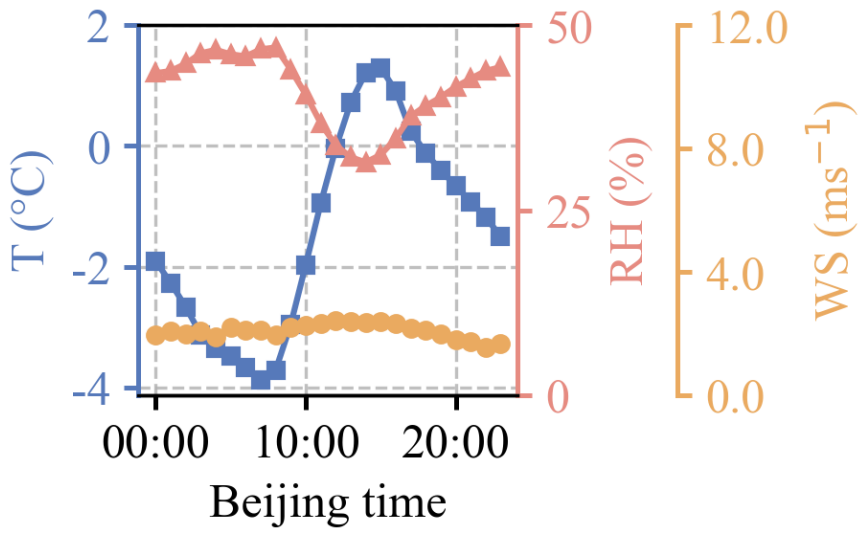

126

127 **Figure S7.** Daily variation of Temperature, Relative Humidity, Wind Speed.

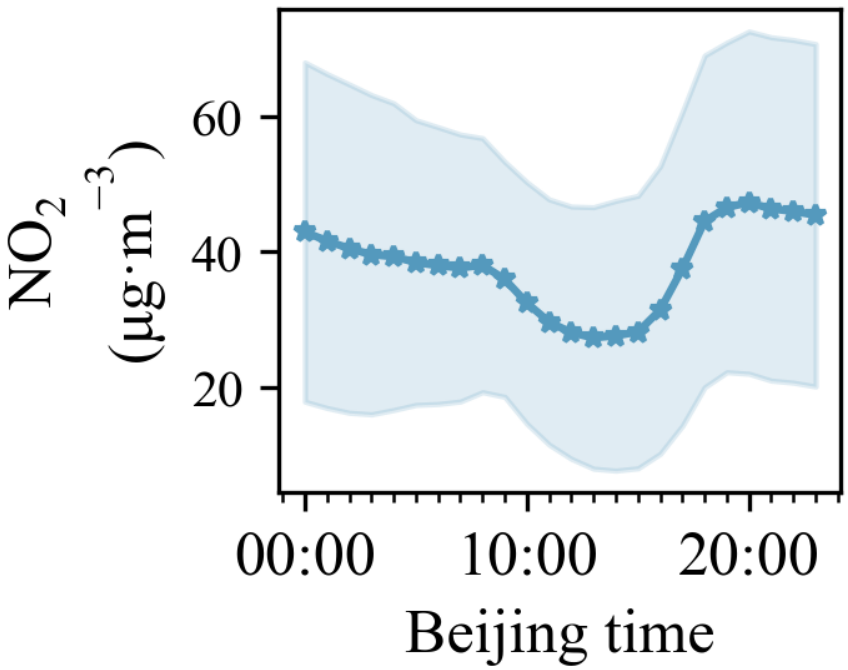

128

129 **Figure S8.** Daily variation of nitrogen dioxide (NO_2). Hourly NO_2 mass concentrations
130 were obtained from the China National Environmental Monitoring Network for the
131 Beijing urban site.

132

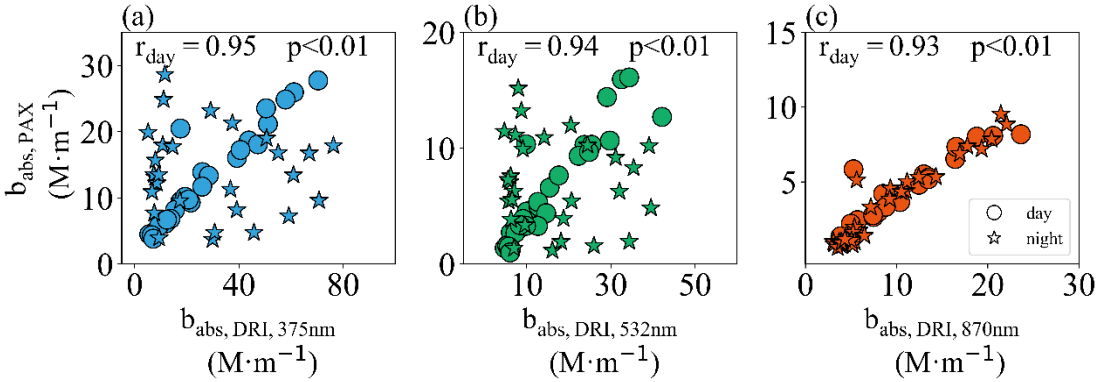

133

134 **Figure S9.** Scatter plots of the aerosol absorption coefficients between PAX and DRI.
135 (a) 375 nm. (b) 532 nm. (c) 870nm.

136

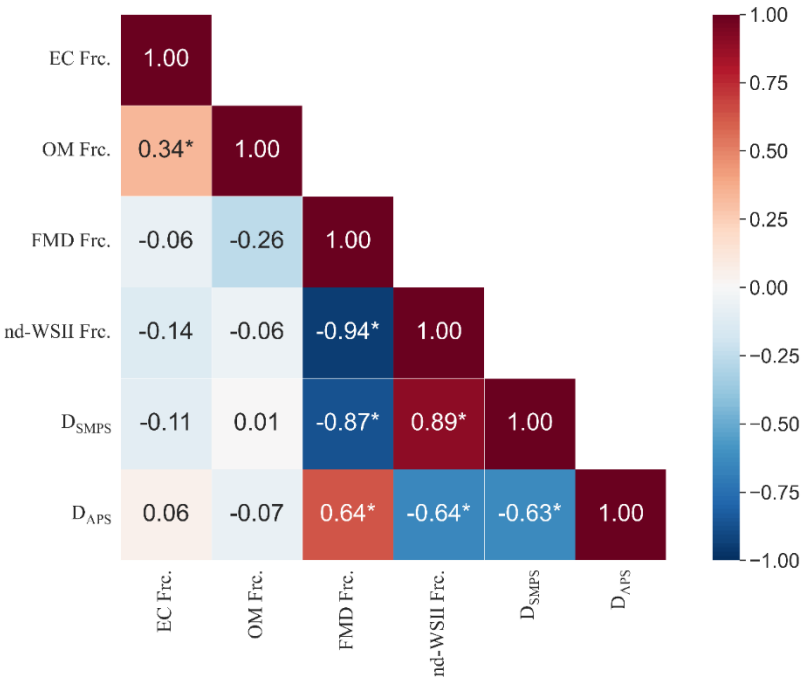

137

138 **Figure S10.** Correlation analysis among chemical composition (non-dust water-soluble

139 ions (nd-WSII), fine mineral dust (FMD), elemental carbon (EC), organic matter (OM))

140 fraction and size parameter (fine-mode mean diameter from SMPS (D_{SMPS}), coarse-

141 mode mean diameter from APS (D_{APS}).

142

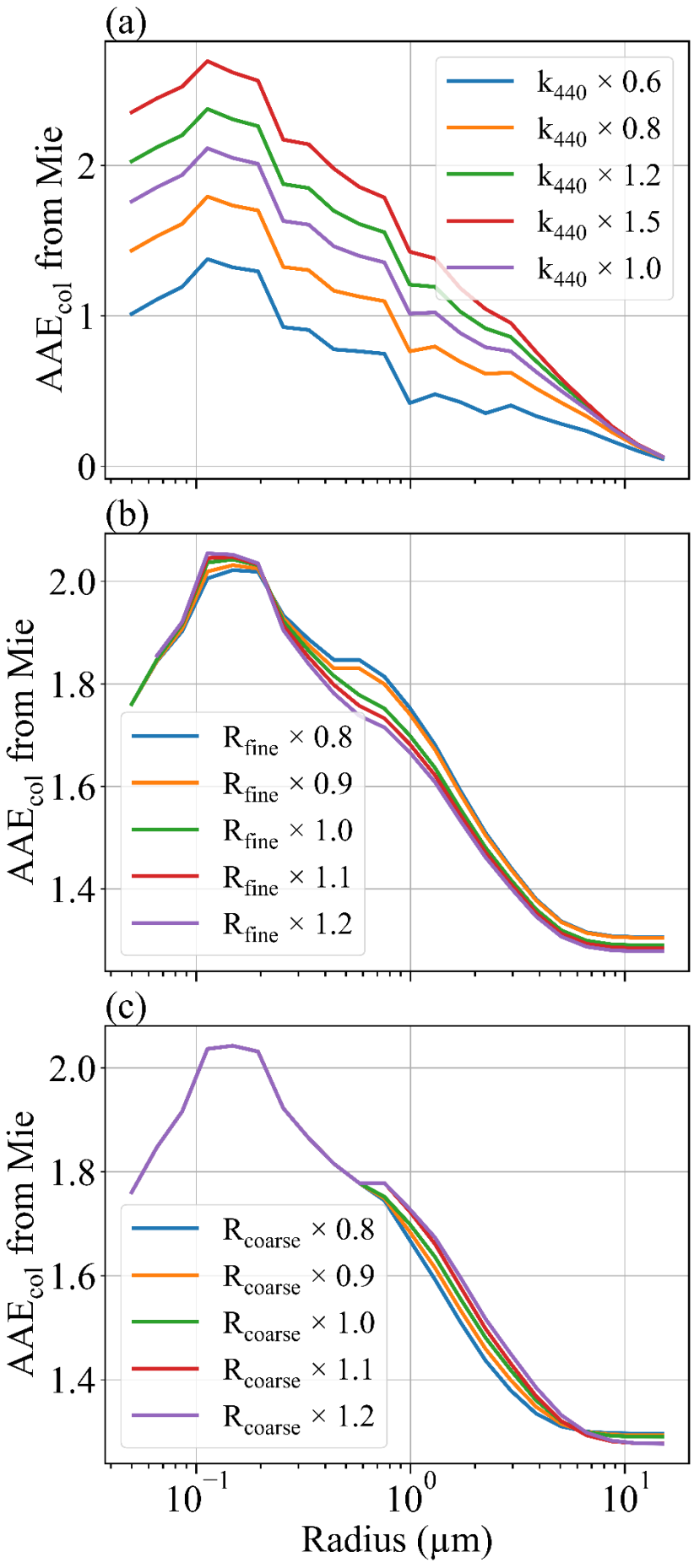
(a)
AAE$_{col}$ from Mie
0
1
2
k$_{440}$ × 0.6
k$_{440}$ × 0.8
k$_{440}$ × 1.2
k$_{440}$ × 1.5
k$_{440}$ × 1.0
(b)
AAE$_{col}$ from Mie
1.4
1.6
1.8
2.0
R$_{fine}$ × 0.8
R$_{fine}$ × 0.9
R$_{fine}$ × 1.0
R$_{fine}$ × 1.1
R$_{fine}$ × 1.2
(c)
AAE$_{col}$ from Mie
1.4
1.6
1.8
2.0
R$_{coarse}$ × 0.8
R$_{coarse}$ × 0.9
R$_{coarse}$ × 1.0
R$_{coarse}$ × 1.1
R$_{coarse}$ × 1.2
10^{-1}
10^{0}
10^{1}
Radius (μm)

143

Figure S11. Mie-theory sensitivity experiments linking composition-related absorptivity and size structure to AAE. (a) Sensitivity to shortwave absorptivity: the imaginary refractive index at 440 nm (k_{440}) is scaled by factors of 0.6, 0.8, 1.0, 1.2, and 1.5 while the size distribution and k_{870} are held fixed (the real part is fixed at n=1.5, the AERONET mean). (b) Sensitivity to fine-mode size: the fine-mode characteristic radius is shifted to 80%, 90%, 100%, 110%, and 120% of its baseline value while conserving the fine-mode integrated volume; the coarse mode is unchanged. (c) Sensitivity to coarse-mode size: the coarse-mode characteristic radius is shifted to the same factors while conserving the coarse-mode integrated volume; the fine mode is unchanged. Curves are shown as a function of particle radius; changes in AAE reflect the differing impacts of absorptivity and size perturbations under otherwise fixed conditions.

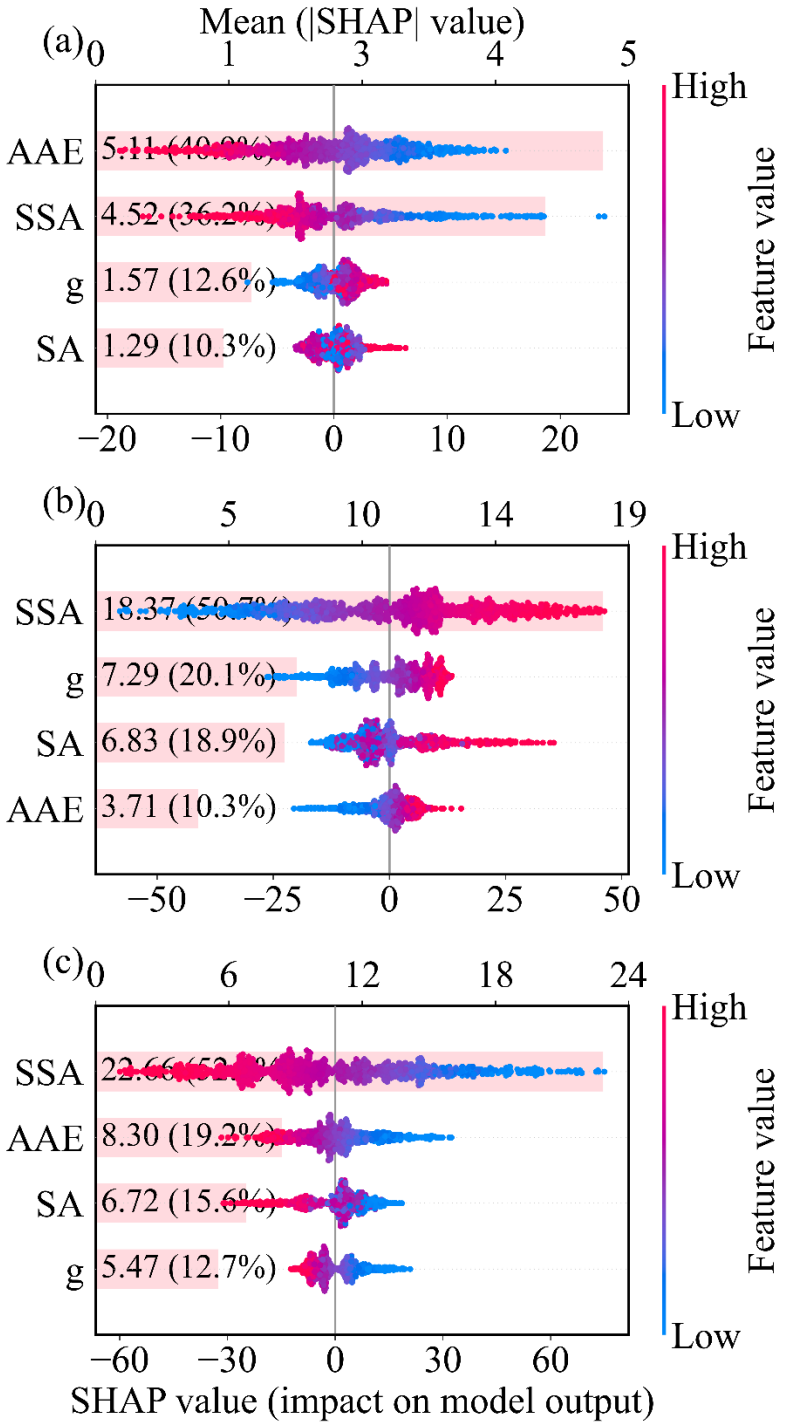

155

156 **Figure S12.** SHAP analysis with AOD fixed at its 25th percentile quantifies the relative
157 contributions of single scattering albedo (SSA), asymmetry parameter (g), surface
158 albedo (SA) and columnar AAE in driving aerosol radiative forcing efficiency (ARFE)
159 variations at the top of the atmosphere (a), bottom (b), and in the atmosphere (c). The

mean absolute SHAP values (numbers in parentheses) indicate the relative contribution of each predictor to the model output.

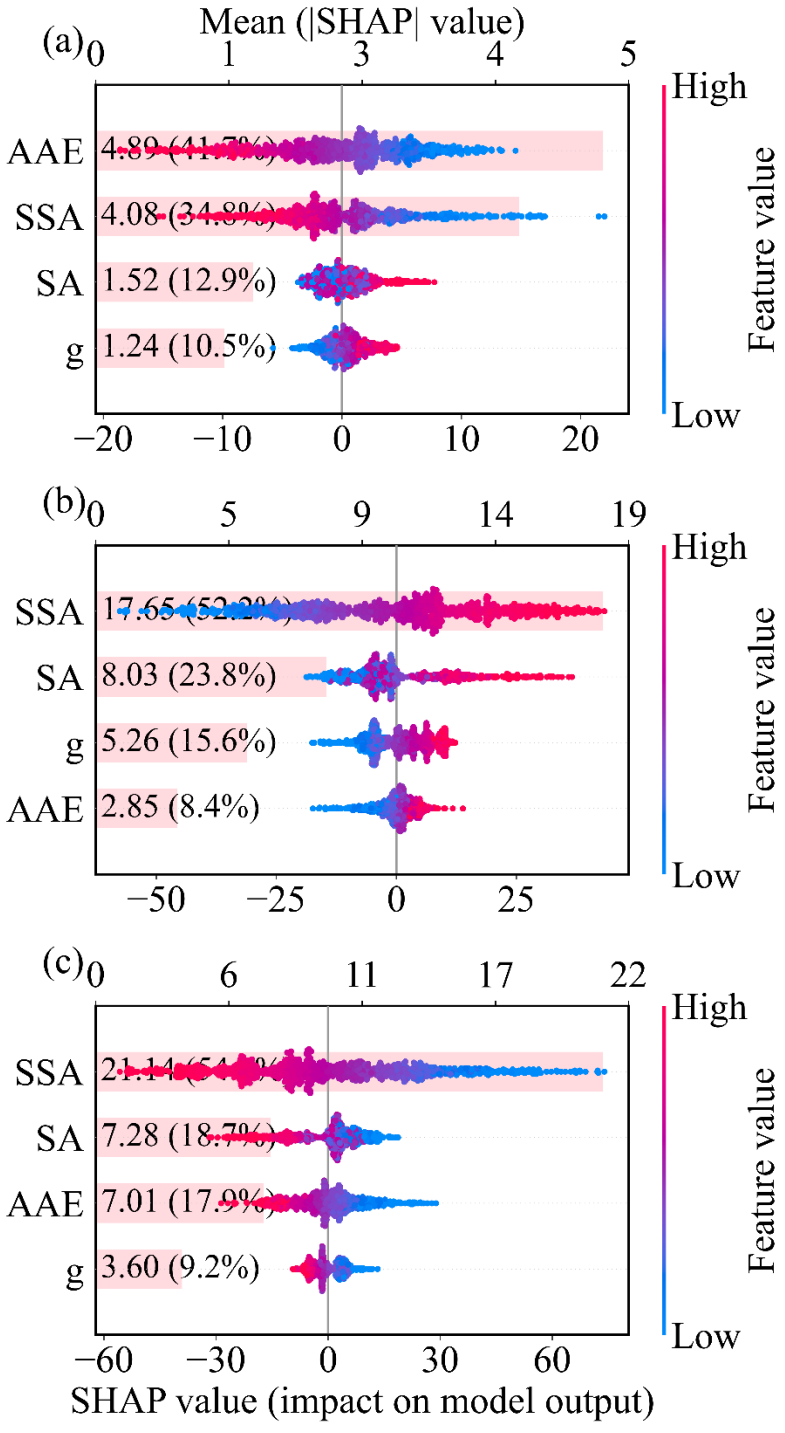

Figure S13. Same as Figure S12, except aerosol optical depth (AOD) is fixed at its 75th percentile.

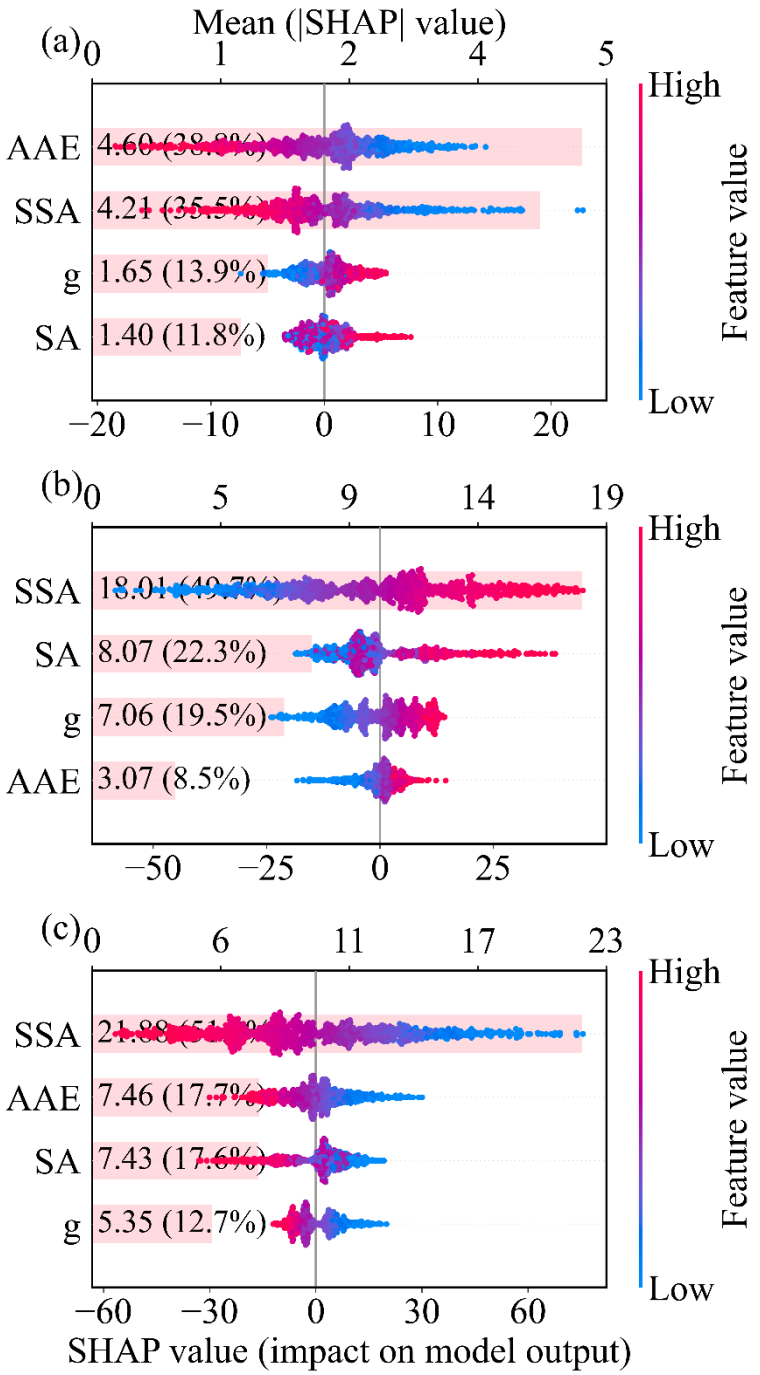

Figure S14. Same as Figure S12, except aerosol optical depth (AOD) is fixed at its mean value.

References

Bohren, C. F. and Huffman, D. R.: *Absorption and Scattering of Light by Small Particles*, John Wiley & Sons, Inc., New York, 1983.

Chow, J. C., Watson, J. G., Chen, L.-W. A., Chang, M. C. O., Robinson, N. F., Trimble, D., and Kohl, S.: The IMPROVE_A Temperature Protocol for Thermal/Optical Carbon Analysis: Maintaining Consistency with a Long-Term Database, Journal of the Air & Waste Management Association, 57, 1014–1023, https://doi.org/10.3155/1047-3289.57.9.1014, 2007.

Shang, D., Hu, M., Zheng, J., Qin, Y., Du, Z., Li, M., Fang, J., Peng, J., Wu, Y., Lu, S., and Guo, S.: Particle number size distribution and new particle formation under the influence of biomass burning at a high-altitude background site at Mt. Yulong (3410 m), China, Atmos. Chem. Phys., 18, 15687–15703, https://doi.org/10.5194/acp-18-15687-2018, 2018.